JOURNAL OF THERMOPHYSICS AND HEAT TRANSFER
Vol. 24, No. 2, April–June 2010

Constrained Vapor Bubble Experiment for International Space Station: Earth's Gravity Results

Arya Chatterjee,* Joel L. Plawsky,† and Peter C. Wayner Jr‡
Rensselaer Polytechnic Institute, Troy, New York 12180
David F. Chao§ and Ronald J. Sicker§
NASA John H. Glenn Research Center at Lewis Field, Cleveland, Ohio 44135
and
Tibor Lorik,¶ Louis Chestney,** John Eustace,†† and John Zoldak‡‡
Zin Technologies, Cleveland, Ohio 44130

DOI: 10.2514/1.47522

The constrained vapor bubble experiment scheduled to fly aboard the International Space Station in the near future promises to give us new insight into the fundamental science of interfacial thermophysics. The evaporating meniscus formed at the corner of the vapor bubble is expected to behave in a significantly different manner in the microgravity environment as compared with the Earth's gravity environment. Since the constrained vapor bubble can also behave as a micro heat pipe, it will additionally help in gaining a technical understanding of the performance of a micro heat pipe in a space environment. Earth-based experiments have been conducted for the past two decades to gain a better knowledge of the rich phenomenon observed in the relatively simple constrained vapor bubble setup. Here, some recent Earth's-gravity-environment-based data obtained on a 30-mm-long constrained vapor bubble have been presented. The data were fitted to a model, and a self-consistent value of the inside heat transfer coefficient was obtained. The external convective and radiative heat transfer coefficients were also determined. These ground-based experiments form a calibration against which the future data from space-based experiments will be compared.

Nomenclature

A_l	=	cross-sectional area of the liquid channel formed by the corner meniscus, m^2
A_v	=	cross-sectional area of the vapor channel formed by the bubble, m^2
g	=	acceleration due to gravity, m^2/s
h_{fg}	=	latent heat of vaporization of working fluid, J/kg
h_{in}	=	internal heat transfer coefficient from solid to the liquid accounting for evaporation, W/m^2 K
h_{out}	=	external heat transfer coefficient from solid to ambient due to natural convection, W/m^2 K
kl_f	=	liquid channel friction factor
kl_v	=	vapor channel friction factor
$L_{l,w}$	=	length of liquid in contact with the wall, thus experiencing shear, m
$L_{v,w}$	=	length of vapor in contact with the wall, thus experiencing shear, m
P_l	=	pressure in the liquid, Pa
P_v	=	pressure in the vapor, Pa
P_{sat}	=	saturation vapor pressure of the working fluid
Q_{in}	=	net heat input, W/m^2
q_e	=	evaporative heat flux per unit length, W/m
r	=	radius of curvature of the corner meniscus at a particular axial location, m
r_0	=	radius of curvature of the corner meniscus at a known axial location, x_0, m
T_{bot}	=	temperature at bottom, K
U_l	=	velocity of the liquid, m/s
U_v	=	velocity of the vapor, m/s
x	=	axial distance, m
ρ_l	=	density of liquid, kg/m^3
σ_l	=	surface tension of the liquid, N/m
$\tau_{l,w}$	=	shear stress between the liquid and the wall, Pa
$\tau_{v,w}$	=	shear stress between the vapor and the wall, Pa

Received 5 October 2009; revision received 16 December 2009; accepted for publication 16 December 2009.

*Graduate Research Assistant, Isermann Department of Chemical and Biological Engineering.
†Professor, Isermann Department of Chemical and Biological Engineering. Member AIAA.
‡Distinguished Research Professor, Isermann Department of Chemical and Biological Engineering. Member AIAA.
§Project Scientist.
¶Project Manager.
**Software Lead.
††Mechanical Lead.
‡‡Systems/Electrical Engineer Lead.

I. Introduction

THE constrained vapor bubble (CVB) is an ideal experimental setup: it lets the investigator study complex phenomenon at multiple scales. It consists of a rather large vapor bubble and a pool of its liquid phase. Both of these are contained in a channel with a rectangular cross section (or other cross sections formed by intersecting flat solid faces) closed at both ends. The system is simple to set up, can be observed by noninvasive methods (such as image analyzing interferometery), has levels of complexity that can be studied in the macroscopic and microscopic realms without fear of one affecting the other, and has immense practical importance as a micro heat pipe.

A CVB is illustrated in Fig. 1. The vapor bubble is constrained within a rectangular solid cavity with the liquid phase separating the vapor from the solid. At one end, the liquid forms a thin film on the flat walls of the solid, and it forms a curved surface at the corners (the menisci). For a perfectly wetting fluid, the walls will be coated with liquid, whereas for a partially wetting fluid, there will be a thin adsorbed layer of vapor that changes the surface interaction between the vapor and the solid. Similar to the perfectly wetting case, the corner meniscus is formed if the fluid is partially wetting. Under closer observation, it becomes apparent that for the case of a perfectly wetting fluid, the liquid completely surrounds the constrained vapor at all places: either with a thin liquid film held in place by attractive

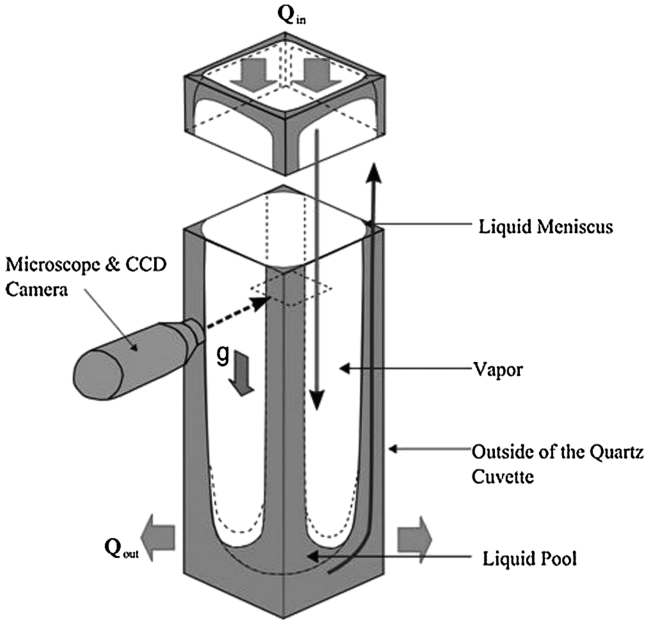

Fig. 1 Constrained vapor bubble and liquid pool.

forces between the wall and the liquid or by a bulk liquid at the corners pushed up there by capillary forces.

Heat pipes are passive heat transfer devices that rely on phase change for transporting heat. The micro heat pipe can be described as a heat pipe for which the capillary radius (inverse of the mean curvature of the liquid–vapor interface) is of the same order as that of the hydraulic radius of the flow channel [1]. The CVB can be thought of as a micro heat pipe, because phase-change phenomena occurring in it can be used to transport heat in a passive manner. Figure 2 shows the functioning of a micro heat pipe for which a quartz cuvette forms the solid wall and an alkane, such as pentane, forms the working fluid. The operating principle of the device remains like a conventional heat pipe; the evaporator region is formed by the region of the CVB containing the bubble, and the condenser is formed by the pool of liquid at the bottom. The heat applied to one end of the heat pipe vaporizes the liquid in that region, and the increasing pressure forces the vapor to move to the cooler end, where it condenses. As shown in the cross-sectional views in Fig. 2, the curvature of the liquid–vapor interface at the corner changes, resulting in capillary pressure pushing the liquid up to the evaporator, thus forming a continuous supply of fresh liquid. Since the corners transport the liquid, no wicking structure is necessary. The heat flux enhancement achieved by these devices is quite large, even though the temperature gradient may be small.

Devices that are essentially CVBs have been studied as micro heat pipes by various researchers [2–17]. The curvature under nonisothermal conditions is different from that of the isothermal (equilibrium) interface curvature because of the phase change in the evaporating section. The interface curvature dynamically adjusts to create a pressure gradient that will allow the liquid to be pumped up the corner. The gradient is such that there is enough liquid left at the top for evaporation, failing which, the heat pipe reaches its performance limit (the capillary limit) and dry-out is said to have occurred. Thus, an unknown factor in many theoretical studies is the interface curvature. The experimental technique developed by Zheng et al. [18] filled this gap by providing this unknown. The interferometry technique gives bulk curvature that provides the most vital clue to the puzzle. With the curvature known, the liquid pressure gradient along the axial direction can be calculated, and thus the fluid flow can be derived. Since the differential amount of fluid is the amount being evaporated, with the knowledge of the flow derived from the curvature data, the heat transfer can be calculated. This forms the cornerstone of our research.

It is thought that the micro heat pipe with relative large internal dimensions will perform better in a microgravity environment. Figure 3. shows a graphical representation of the pressure profile distribution in a heat pipe [1]. It can be seen that the absence of body forces reduces the pressure difference between the vapor and the liquid, thus increasing the capillary limit, which means that the heat pipe can transport more heat. Using the model developed by Huang et al. [19], the maximum heat flux without dry-out had been calculated by Basu et al. [20] for a 22 mm vapor bubble in the Earth's environment and in microgravity. The curvature in the Earth's environment is compared with those predicted for microgravity in Fig. 4. It was shown by Basu et al. [20]. that the same device might be able to dissipate 60 times more power in a microgravity environment.

In this paper, data in Earth's gravity environment from the CVB experiment that is destined to fly on the International Space Station have been presented. For the first time, high-resolution image data of the inside surface of the cuvette at isothermal conditions and at various heat fluxes have been obtained. Temperature data of the outside surface were also collected, and a model was developed to match the temperature data and meniscus curvature.

II. NASA CVB Experimental Setup

These experiments were performed as part of the ground-run calibration using the same CVB experimental apparatus that is to be flown aboard the International Space Station (ISS). The hardware has been developed by NASA and ZinTech as part of a series of experiments in basic fluid physics and is to be housed in the Fluids

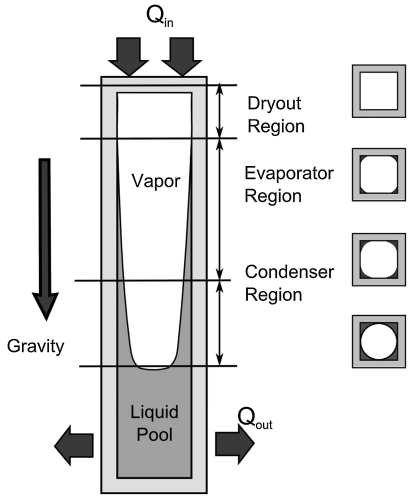

Fig. 2 CVB as a micro heat pipe. the dry-out region is due to the heat flux Q_{in} exceeding the capillary limit. The cross-sectional views show the changing liquid curvature.

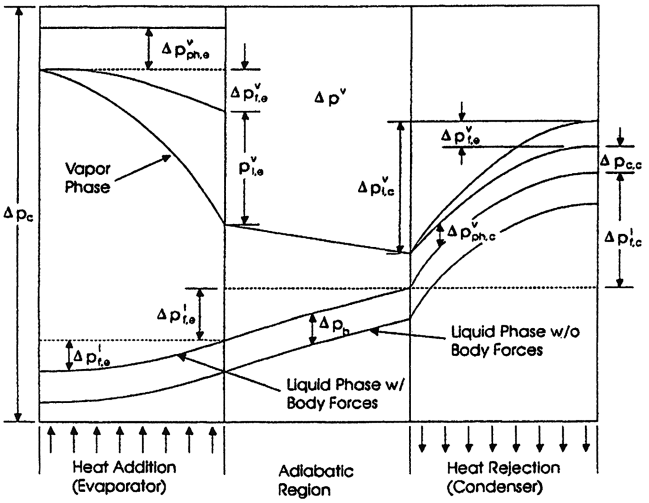

Fig. 3 Graphical representation of the pressure drops in a heat pipe (from Peterson [1]).

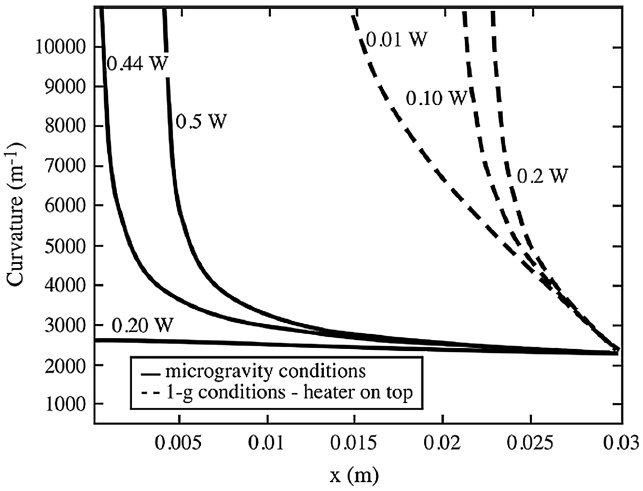

Fig. 4 Axial curvature gradients as a function of heat input for microgravity and Earth gravity conditions (from Basu et al. [20]).

Integrated Rack (FIR) onboard the ISS. The Light Microscopy Module (LMM), developed as a part of the FIR, consists of a completely automated optical microscope that can be used to perform a variety of experiments. It is designed to accept small-sized (about the size of a paperback) modules that an astronaut can load onto it. Once loaded, the experiment can be conducted remotely by operators from Earth. One of the first experiments scheduled to be performed using the LMM is the CVB. Figure 5 shows the setup of the FIR, in which the CVB is built as a small module that can be one of the payloads for the LMM. As part of the experimental matrix, ground-based experiments are required that will be compared with experiments in space conducted at the same heater and cooler settings. The results described here are part of one such ground-based study.

A. Description of the Assembly

The CVB has been built in a modular fashion for easy insertion into the LMM by an astronaut. A schematic is shown in Fig. 6. The assembly consisted of a quartz (see Fig. 1) cuvette that was closed at one end. The cuvette cavity was 3×3 mm on the inside, with a bubble length of 20 mm. Other assemblies also part of the CVB experiment have bubbles that are 30 and 40 mm long. The thickness of the cuvette wall was 1.25 mm, making the outside dimension 5.5×5.5 mm. These were spectrophotometer cuvettes that were manufactured to very-high-tolerance specifications by the manufacturer for the CVB experiment. Specifically, they had sharp corners, extremely flat surfaces, and square cross sections. The quartz is transparent at visible wavelengths but is a blackbody at thermal wavelengths [20]. At the closed end of the cuvette, a heater was attached that allowed us to perform nonisothermal studies. The heater was insulated from all sides to ensure that all the electrical

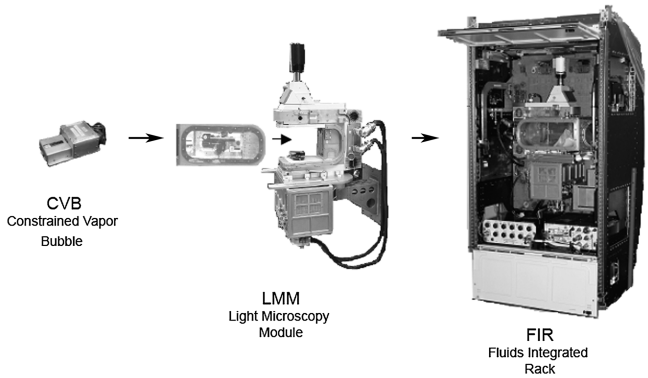

Fig. 5 CVB experiment can be inserted into the LMM, which in turn goes inside the FIR, which will be one of the science experiment racks in the ISS.

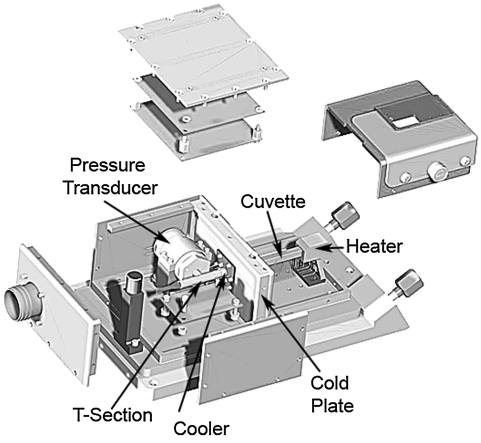

Fig. 6 Schematic of the CVB assembly. The module has its own electronics and control units to enable easy insertion into the LMM.

energy supplied to the heater flowed into the cuvette. The open end of the cuvette was sealed using a cold finger that was kept at a known constant low temperature and that served to drain the heat away to a large copper heat sink. The cold finger was made of Invar to have a thermal expansion coefficient similar to that of quartz. Thermoelectric coolers attached to the cold finger end actively removed heat from the cuvette and drew it off into the heat sink that was cooled by circulating cold water. The cold end of the cuvette can be maintained at a prespecified temperature using the thermoelectric coolers. Stainless steel pipes attached to the other end of the cold finger formed a T section, one end of which terminated in a pressure transducer, and a valve was attached to the other end. This valve was used to load the system with the working fluid and then closed off. The cold finger had tiny holes drilled through it that connected the space in the cuvette on one side to the space in the piping on the other. The cavity formed by the piping and the cuvette was partially filled with pentane, resulting in a vapor bubble remaining inside the cuvette. To measure temperature, thermocouples were attached to the outside surface of the quartz cuvette by drilling holes into the surface of the quartz. Pressure was measured using the pressure transducer.

B. How the Experiment is Run: SW Setup

The experiments have been completely automated, since they would have been too long to be performed by an astronaut. Thus, scripts written in a computer language are run to perform the experiment and collect the scientific data. There are three main computers in the LMM: the image processing and storage unit, the fluid science avionics package, and the input–output processor. Together, they collect the temperature, pressure, and image data during the experiment. All data are transmitted at the end of the experiment to a separate computer system. During space experiments, the data will similarly be transmitted to Earth. Telemetry received during the running of the experiment ensures that it is progressing as planned, and guidelines on maximum allowable temperature and pressure ensure a safe experiment. Each nonisothermal experimental run has two phases: a transient phase, when the heater power is slowly ramped up and the temperature and pressure approach a steady state, and a data-acquisition phase. Once a set of criteria has been satisfied, signifying that steady state has been reached, the experiment goes into data-acquisition mode and the temperature, pressure, and image data are acquired.

C. Image Acquisition

The inside surface of the cuvette can be viewed through the microscope. The CVB module can be easily inserted into the light microscopy module. Inside the LMM, the module is mounted on an x, y, and z translation stage. The x and y translate the assembly, and the z movement adjusts focus. Focus is found by a contrast-enhancement algorithm whereby the image with the maximum contrast is taken to be the focused image. The entire LMM can be

tilted around its axis so that the cuvette assembly can be oriented perpendicularly or horizontally to gravity.

The full length of the cuvette can also be viewed using a surveillance camera. These images, captured at the beginning and end of each experimental cycle, ensure that the experiment is progressing correctly and that some liquid pool remains inside the cuvette. One such surveillance image is shown in Fig. 7. The thermocouples are visible and the liquid pentane pool can be seen near the cold finger. From the location of the thermocouples, the sizes of the bubble and the liquid pool can be estimated.

D. Temperature Data Acquisition

The temperature data were collected using the thermocouples that have been embedded into the surface of the cuvette. Of the four sides of the cuvette, the side to be viewed through the microscope was kept bare. Most of the thermocouples were attached on the side opposite to that being viewed by the microscope, with additional thermocouples also attached on the two remaining sides. The thermocouple positions along the axis of the cuvette are shown in Fig. 8. The thermocouples had a stated accuracy of $\pm 0.5°C$. During the transient phase, readings were recorded every 1 min, and during data-acquisition mode readings came at 2.40 s intervals. This rate of acquisition was chosen since there are 24 pairs of multiplexed data lines and data are acquired at 100 ms intervals between each line. The pressure transducer data were collected at the same time intervals as the thermocouple data. The pressure transducer had a range of 5.4 to 19.3 psi with an accuracy of ± 0.1 psi. Along with this data, some additional information such as the electrical power input to the heater, the power supplied to the thermoelectric coolers, etc., was also recorded.

For the present study, the experiments in the Earth's gravity environment were performed in two steps. The cuvette was aligned vertically with the gravitational field acting from the heater toward the cooler. In the first step, the cuvette was kept isothermal and no electrical energy was applied to the heater or cooler. This isothermal experiment served as a calibration, whereby the validity of the Young–Laplace equation could be determined. Next, a series of nonisothermal runs were performed with the cooler set to a specified cold temperature (15°C) and various heater powers supplied to the heater.

E. Data Processing for Temperature Data

The thermocouples have a very high-spatial-resolution and, during the data-acquisition phase, a very high temporal resolution as well. The high accuracy of the data allowed us to determine the spatial temperature gradient. Figure 9 shows the temperature profile along the cuvette during the initial transient and the subsequent data-acquisition phase for a typical run. For locations near the top of the cuvette, the temperature rose initially before settling to a constant value. The temperature at the cooler end remained constant at the set value. The experiment phase (data acquisition) was started after about 20 min. To calculate the spatial derivative of the temperature profile, the last few (here, 20) readings were averaged to reduce inherent noise. This averaged temperature profile was fitted to a smoothing cubic spline, and a subsequent derivative was taken to obtain the temperature gradient. Figure 10a shows the variation of temperature with location during a run when the heater input was set at 0.4 W. Distance is measured from the top of the cuvette (including the top closed end). A maximum of 0.3% standard deviation was shown by the temperature data that were considered for determining the spatial derivative. Figure 10b shows the temperature gradient along the cuvette. It can be seen that the spatial derivative of the temperature changed its slope twice. The position of the first change

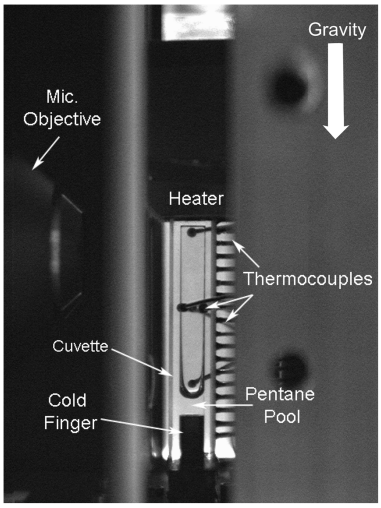

Fig. 7 Surveillance image of the CVB. The various components have been labeled. The working fluid is pentane.

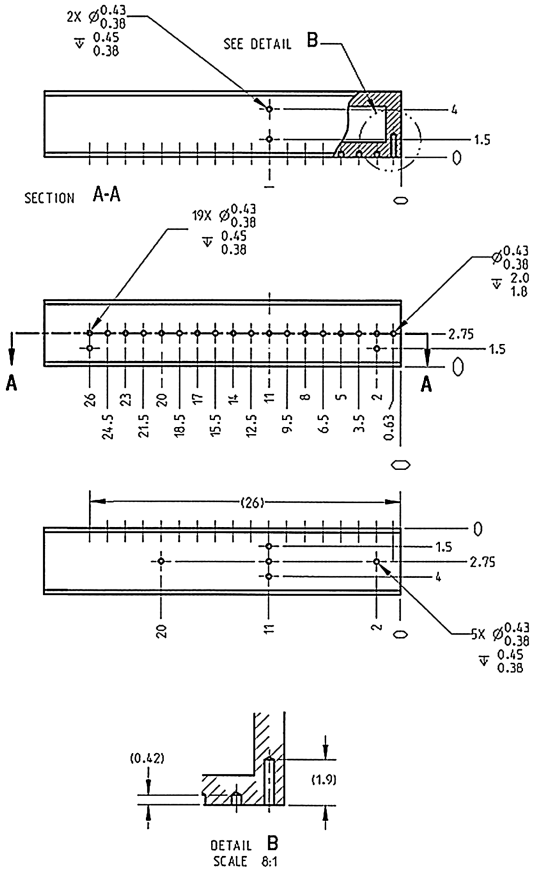

Fig. 8 Thermocouple placement on the cuvette surface. To obtain good thermal contact, the thermocouples were embedded in holes drilled into the quartz wall of the cuvette. All dimensions are in millimeters.

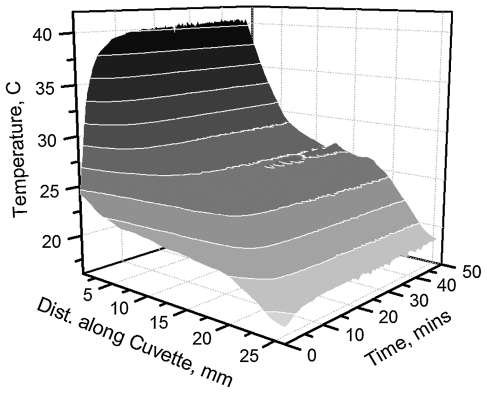

Fig. 9 Temperature measurement from various thermocouples along the axial location of the cuvette plotted in time for one of the runs. The temperature readings reach steady state after about 20 min.

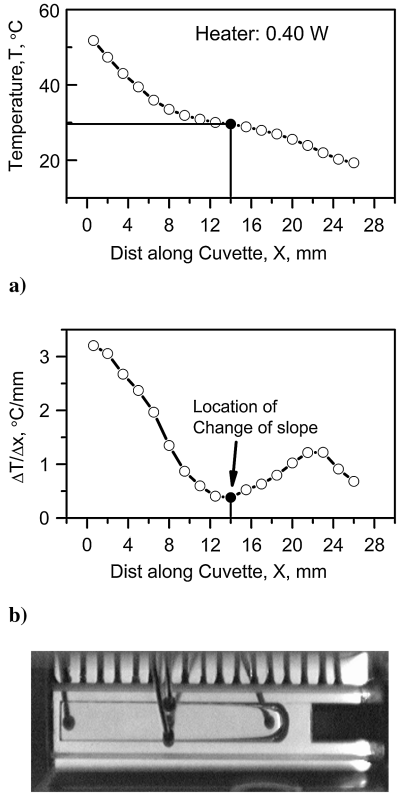

Fig. 10 Data for a heater input of 0.40 W: a) temperature at various axial locations along the cuvette for a typical run, b) temperature derivative with distance obtained from by differentiating a spline fit of the data (location of the change of slope is shown), and c) cuvette to help correlate the thermocouple positions with the data.

in slope corresponded with the beginning of the condenser region of a typical heat pipe and will be discussed in detail later. The position of the second change in slope (around the 21.5 mm mark) corresponded with the beginning of the liquid pool and the cold finger. The accompanying change in thermal conductivity caused the change in slope. Pressure data were similarly computed by taking a mean of the pressure reading from the pressure transducer for the last 20 data points.

F. Data Processing for Image Data

The image data for the experiments were collected by an automated script that moved the CVB assembly to predetermined locations along the cuvette and also brought the inner surface into focus. A relatively low magnification was used ($10x$) to take these images, thus allowing a higher depth of field and less refocusing upon moving to a new location. Since the location of the corner meniscus could not be predicted, images were taken such that more than half of the entire inside surface of the cuvette facing the microscope could be mapped. This was done by capturing three consecutive images at each X location, where X is in the direction from the heater end to the cooler end. These images at the three locations can then be joined together by means of an image-processing algorithm such that a composite image is generated. Such composites at each X location can then be further stitched to create a composite image of the entire inside surface of the cuvette. Figure 11 shows the composite image generated for a typical run.

Figure 12 shows the relationship between the local interface curvature of the corner meniscus and the projected length of the meniscus on the solid surface. The interface curvature at a given axial location is given by

$$K = \left(\frac{1}{R_{Ax}} + \frac{1}{R_{Tv}}\right) \tag{1}$$

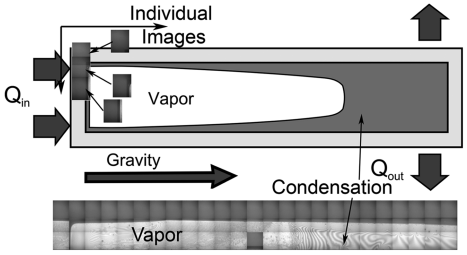

Fig. 11 Formation of a typical composite image showing the various zones corresponding to the CVB schematic.

where R_{Ax} is the radius of curvature in the axial direction and R_{Tv} is radius of curvature in the perpendicular (transverse) direction. Assuming that the local interface curvature of the corner meniscus surface has a relatively low component along the axial direction (R_{Ax} is large), it can be shown that the meniscus resembles a circle of radius R_{Tv} intersecting a right angle, with the two arms of the angle being tangent to the circle. This is particularly true for perfectly wetting fluids for which the contact angle is sufficiently small to be considered close to zero. Then it is easy to see that the length of the wetted surface is equal to the radius of the circle, and thus the inverse of the circle gives the curvature of the liquid–vapor interface. This is a straightforward way to determine interface curvature of the meniscus using low-magnification data. It was noted earlier that a thin film of liquid remains adsorbed on the surface of the quartz. Although this would indicate that there is no sharp junction between the three phases, for the purpose of axial curvature gradient calculation in the macroscopic scale, it can be assumed that a well-defined contact line exits. Applying image-processing techniques on the composite image of the inside surface of the cuvette generated earlier, the edge of the meniscus can be determined. The edge of the quartz substrate can be identified by noting that it forms a sharp boundary. A typical sequence of edge identification to determine thickness is shown in Fig. 13. Figure 13a shows the composite image of the top corner of the cuvette on which one can clearly see the edge of the liquid meniscus at upper and side corners. The outline of the quartz cuvette is also visible. Figure 13b shows the processed image in which the edge has been identified correctly by the image-processing algorithm. Figure 13c shows the original image with the meniscus edge and the quartz surface delineated. Once the edge of the meniscus is known in this manner, the distance from the corner can be easily calculated and this gives the curvature with very high accuracy at all axial locations of the heat pipe.

III. Experimental Results from NASA CVB Experiment

In this section, data from isothermal and nonisothermal experiments performed in the Earth's gravity environment are presented.

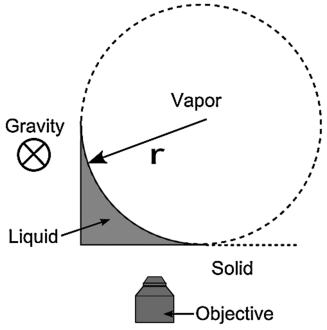

Fig. 12 Corner meniscus for a perfectly wetting fluid (where the contact angle is small) can be imagined to be a circle touching the side walls. The projection of the circle can thus provide us the curvature ($1/r$). Gravity is acting into the page, such that the cross section of the cuvette is visible.

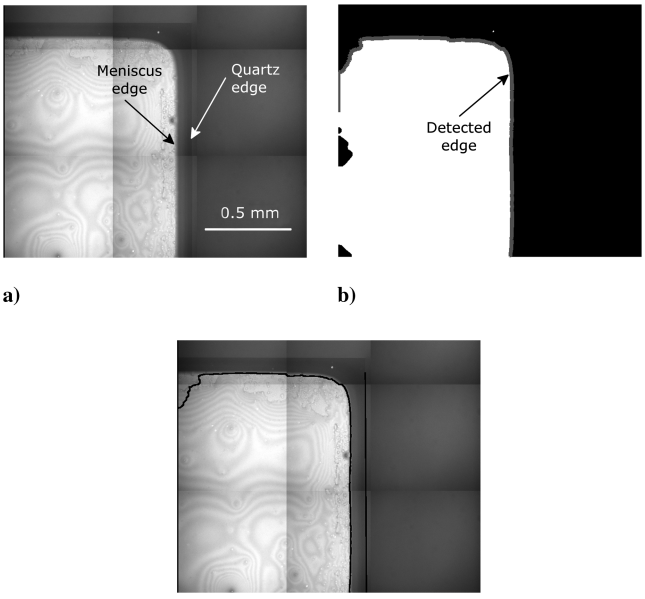

Fig. 13 Image processing steps: a) portion of the composite image obtained by stitching individual images, b) image-processing algorithms identifies the inside edge of the corner meniscus (gray line), and c) edge detected by the algorithm superimposed on the original image. The edge of the quartz cuvette is also plotted. The distance between the detected edge and the wall can be used to calculate the curvature of the corner meniscus.

A. Isothermal Data: Agreement with Young–Laplace Equation

For the isothermal experiment, the heater and the cooler were both turned off and the inside surface of the cuvette was imaged, as shown in Fig. 14a. Because of a bug in the computer program, certain images got repeated and show up as such in the final composite image. Luckily, most of these repeat images fell in the solid quartz part of the cuvette and it was possible to extract the edge of the liquid meniscus using the image-processing method described in Sec. II.

The Young–Laplace equation gives

$$P_v - P_l = \frac{\sigma_l}{r} \tag{2}$$

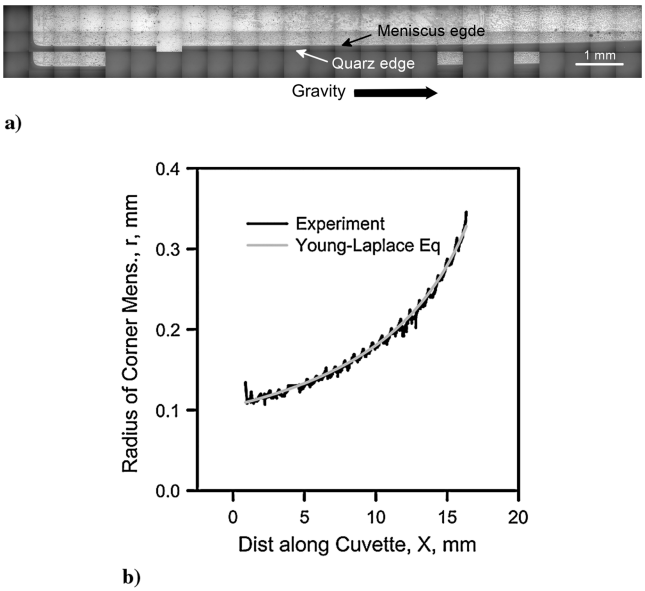

Fig. 14 Isothermal condition data: a) composite image of the corner meniscus of 20 mm NASA cuvette at $1-g$ using 10x magnification and b) Young–Laplace equation was used to compare the experimental data with Eq. (4). Gravity is acting from left to right.

where P_v is the pressure in the vapor, P_l is the pressure in the liquid, σ_l is the surface tension of the liquid (assumed to be constant, though the authors acknowledge that in the microgravity environment, thermocapillary effects would be significant), and r is the radius of curvature of the meniscus at the axial location X. For the isothermal case, neglecting the variation of curvature along the transverse direction (i.e., assuming that the meniscus cross section is circular) and assuming that curvature varies because of the change in radius of circle formed by the meniscus,

$$\frac{\mathrm{d}P_v}{\mathrm{d}X} - \frac{\mathrm{d}P_l}{\mathrm{d}X} = -\frac{\sigma_l}{r^2}\frac{\mathrm{d}r}{\mathrm{d}X} \tag{3}$$

For the isothermal case, the pressure in the vapor can be assumed to be constant (the vapor density is negligible compared with liquid density), and the pressure in the liquid is merely the hydrostatic pressure. Thus, the radius is given by

$$r = 1\Big/\left(\frac{\rho_l g(X_0 - X)}{\sigma_l} + \frac{1}{r_0}\right) \tag{4}$$

where r_0 is the radius at the axial location X_0. Figure 14b shows excellent agreement of the isothermal profile from the experiment with the theoretical value predicted by Eq. (4). Here, the value of r_0 was taken from an arbitrary point X_0 in the experimental data. The authors acknowledge that the equivalence of the theory and experiment merely reflects that the Young–Laplace relation describes the phenomena, and an independent proof similar to that given by Wong et al. [21] is required and is proposed as part of the future work.

B. Nonisothermal Data: Formation of Zones

For the nonisothermal experiment, the cooler was set at 15°C and the heater was set at various preset energy input levels. In all heater settings, some characteristic trends of temperature, pressure, and internal-liquid profile were observed.

Figure 15 shows the various zones identified in the nonisothermal cuvette liquid flow at 0.40 W heater input. The top region, zone 1, corresponds to the evaporator region near the heater; the middle, zone 2, corresponds to the intermediate region [22]; and the bottom, zone 3, corresponds to the condenser region of a typical heat pipe. Zone 3 is easily identified by the presence of condensate on the side wall, as evident from the fringes. A fourth zone, zone 4, consisting of a central drop region, was also seen to form. This drop consists of pentane, and upon using higher magnification, it is revealed that there is a thin line of liquid connecting it to the corner meniscus.

C. Nonisothermal Data: Movement of the Zones

With the change of heater power, it was noticed that the various zones shifted position. Figure 16 shows the position of the four zones at various heater powers indicated by the numbers on the left corner of each composite image. The white arrows mark the location of the beginning of zone 3, or the condensation section. The beginning of the region of condensation moved away from the heater end (left side) and toward the cooler end (right side) with increasing heater input. Thus, if one estimated the effective length of the condenser as being from the beginning of the condenser region to the top of the liquid pool, which would lie further to the right of Fig. 16 and for which the position remains constant at all heat fluxes, one would conclude that the total length of the condenser region decreased with increasing heat input.

Similar to the shift of the condenser region, zone 4 (the central drop on the surface of the cuvette wall) also shifted downward. The

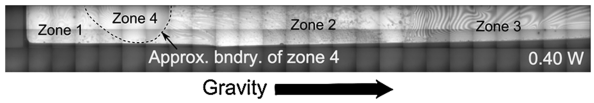

Fig. 15 Composite image of corner meniscus of 20 mm NASA cuvette at $1-g$ using 10x magnification at 0.40 W heater input. The various zones are marked (see text for details). Gravity is acting from left to right.

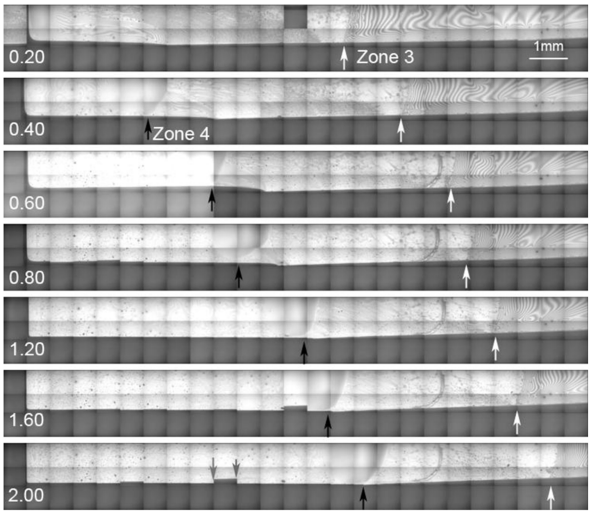

Fig. 16 The movement of the location of zone 3 (condenser region for the heat pipe) and zone 4 (central drop) with increasing heater power. Heater power for each composite image is given on the lower left corner. Gravity is acting from left to right.

approximate position of the central drop is marked in Fig. 16 by a black arrow. A distinct drop was not observed in the case of a 0.20 W heater input. The drop size seemed to be more or less constant at all heat inputs.

The image data were processed using the algorithm described above, and the edge of the corner meniscus was determined; these are plotted in Fig. 17a for different input heat fluxes. The presence of the drop (zone 4) caused the meniscus to be pinched at a location a little further down from the location of the drop, toward the cooler end of the heat pipe. In this initial paper, we conjecture that the drop is being formed due to the presence of a local cold spot on the quartz surface, the location of which is a function of the heater input. The drop could be the result of vapor condensing on this cold spot because of the lower relative local vapor pressure in the liquid. Increasing the magnification to study the drop region, it was revealed that the fluid flow was very complicated, and microconvection currents might exist that supplied the drop with fluid from the corner meniscus. The validity of this hypothesis will be tested by further experiments in the microgravity environment, in which convection will be absent.

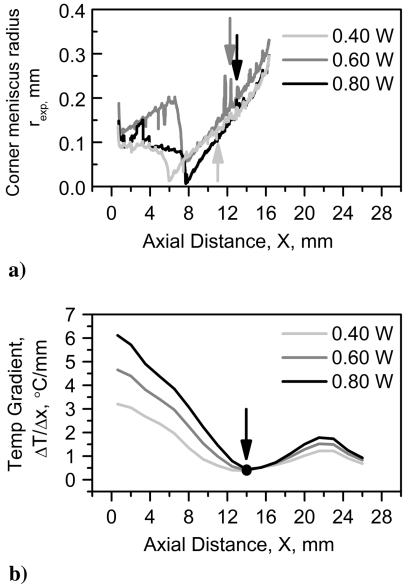

Fig. 17 Plots of a) corner meniscus thickness extracted from the experimental data with the arrows marking the beginning of zone 3 and b) minimum in the temperature gradient indicating the start of the condenser of the heat pipe.

D. Nonisothermal Data: Temperature–Condenser-Region Location Correlation

The high-accuracy and high-spatial-resolution temperature profile allows us to calculate the spatial temperature gradient. Figure 17 shows the correlation between the positions of the beginning of zone 3 (condenser region) with the change in the slope of the temperature profile gradient. The arrows in Fig. 17a mark the beginning of zone 3 from the imaging data (i.e., the location of the white arrows in Fig. 16). The arrow in Fig. 17b marks the location at which the temperature gradient profile changes slope. The location happens to be the same in the three heat fluxes shown. There is a strong correlation between the positions. The reader is reminded that temperature data were collected only at discrete points on the surface of the quartz cuvette, and hence the temperature gradient was evaluated only at those points, whereas the image data have much higher spatial resolution.

E. Nonisothermal Data: Pressure-Temperature Correlation

It is expected that the pressure in the pentane vapor space is almost uniform [23]. Since the vapor just begins to condense at the start of the condenser, the vapor pressure of pentane at the temperature corresponding to this location should be equal to the pressure of the pentane vapor in the bubble. The spatial derivative of temperature was evaluated and the location of the change in slope of the temperature gradient was determined, as outlined in the previous section. Since this corresponds well with the beginning of the condenser region, the temperature corresponding to the change of slope location, i.e., where the temperature gradient reaches a minimum (see Fig. 17b), was used to calculate the vapor pressure of pentane according to the Antoine equation:

$$\log_{10}(P) = A - \frac{B}{(T + C)} \tag{5}$$

where A, B, and C are constants given in Table 1, and P_l is the vapor pressure of the liquid at temperature T (in °C). Figure 18 shows that there is a very good correlation between the pressure from the above calculation with the pressure measured experimentally.

F. Nonisothermal Data: Oscillations

At higher values of heat input, the corner meniscus began to oscillate. This was apparent from the discontinuities that were visible in the composite image. Since the camera translates along the axis and takes images at each axial location, the images in the composite are taken at different times. Thus, the camera captured the meniscus in various phases of the oscillations. This makes the final composite image look discontinuous, depending on whether the meniscus was at a receded or advanced state at the time of image acquisition. The oscillations were later captured by using video mode of the camera and their existence was confirmed.

IV. Theoretical Modeling of Nonisothermal Heat Pipe

Many models for micro heat pipe [3–8,10–14,19,20] exist in literature. Although wicked heat pipes use Darcy's law to model the transport in the porous material, wickless heat pipes use the Young–Laplace equation to calculate the liquid pressure gradient. Sometimes, the vapor phase may be neglected altogether, since the vapor phase is usually very large and has very low density. Thus, the

Table 1 Antoine coefficients for pentane

	Antoine equation coefficients			Validity range	
Material	A	B	C	$T_{\min}$, °C	$T_{\max}$, °C
Pentane	7.00877	1134.15	238.678	−129.73	196.5

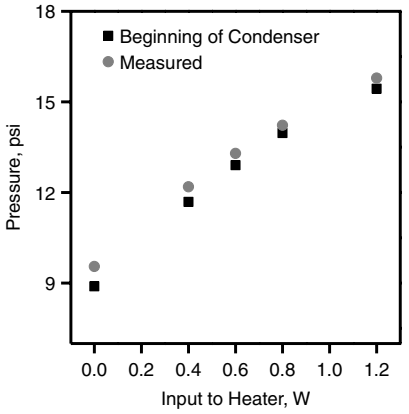

Fig. 18 A strong correlation exists between the vapor pressure measured experimentally and the vapor pressure at the beginning of the condenser region.

pressure gradient is lower in the vapor phase. Some of the assumptions made here are as follows:

1) The system is in steady state.
2) The vapor temperature is a constant and is T_v.
3) Fluid properties are constant ($\rho_l, \sigma_l, \mu_l, \rho_v, \sigma_v, \mu_v$).
4) The flow is laminar and the fluid is incompressible.

There is a single radius of curvature at a given axial location, even though the radius of curvature is clearly changing axially. This is justified because the curvature in the axial direction is very small.

Here, a one-dimensional fluid flow model coupled with a two-dimensional heat transfer model for the flow of heat in the solid has been presented. Considering the fluid flow, the Young–Laplace equation (3) gives the pressure gradient, and the equation for conservation of mass for the liquid phase is given by

$$\rho_l U_l \frac{\mathrm{d}A_l}{\mathrm{d}X} + \rho_l A_l \frac{\mathrm{d}U_l}{\mathrm{d}X} - \frac{q_e}{h_{fg}} = 0 \tag{6}$$

In the vapor phase, we have

$$\rho_v U_v \frac{\mathrm{d}A_v}{\mathrm{d}X} + \rho_v A_v \frac{\mathrm{d}U_v}{\mathrm{d}X} + \frac{q_e}{h_{fg}} = 0 \tag{7}$$

where U_l is the average liquid velocity, U_v is the velocity in the vapor, A_l is the area of the liquid cross section, A_v is the area of the vapor cross section, and X is the axial location. Since the total cross-sectional area of the cuvette is a constant (3×3 mm), the area of the vapor can be calculated by subtracting the area of the liquid from this constant. In Eq. (6), q_e is the evaporative heat flux (or, in the condenser region, the condensation heat flux), and h_{fg} is the latent heat of vaporization of pentane. The value of A_l comes from geometric considerations and is given by

$$A_l = 2C_l r^2 \tag{8}$$

where

$$C_l = \frac{\sin(\alpha)\sin(\phi/2)}{\sin^2(\alpha/2)} - \phi + \sin(\phi) \tag{9}$$

Here, α is the vertex angle of the groove $\pi/2$ in our case, and $\phi = \pi/2 - 2\theta_c$, where θ_c is the contact angle, assumed to be zero here.

Likewise, the equations for the conservation of momentum are

$$A_l \frac{\mathrm{d}P_l}{\mathrm{d}X} + \rho_l g A_l \sin(\beta) + \rho_l U_l^2 \frac{\mathrm{d}A_l}{\mathrm{d}X} + 2\rho_l A_l U_l \frac{\mathrm{d}U_l}{\mathrm{d}X} - L_{l,w}\tau_{l,w} = 0 \tag{10}$$

and

$$A_v \frac{\mathrm{d}P_v}{\mathrm{d}X} + \rho_v g A_v \sin(\beta) + \rho_v U_v^2 \frac{\mathrm{d}A_v}{\mathrm{d}X} + 2\rho_v A_v U_v \frac{\mathrm{d}U_v}{\mathrm{d}X} + L_{v,w}\tau_{v,w} = 0 \tag{11}$$

for the liquid and vapor phases, respectively. Here, g is the acceleration due to gravity and β is the inclination of the cuvette to the horizontal ($\pi/2$ for our vertically aligned case), $\tau_{l,w}$ is the wall shear stress for the liquid, $L_{l,w}$ is the surface of the wall in contact with the liquid, and $\tau_{v,w}$ and $L_{v,w}$ are the corresponding quantities for the vapor phase. The interphase shear stress has been neglected. Although other authors [5] have shown that the interfacial shear stress can be important, they can be neglected in this initial study, since the relative velocity between the liquid and the vapor phases in our system was low. Adhesion effects can also be neglected, since the film thickness is very large.

The shear stress at the wall is based on friction factors, and for the liquid phase it is given by

$$\tau_{l,w} = \frac{k l_f L_{l,w} \mu_l}{16 A_l \rho_l} \tag{12}$$

where k_{lf} is the friction factor for the liquid and is equal to 13.1 as given by Ayyaswamy et al. [24]. A similar equation exists for the vapor phase with a friction factor of 15.1 for a square cross section. Here, it has been assumed that the small area occupied by the liquid meniscii at the four corners of the square channel does not significantly affect the value of the friction factor.

These ordinary differential equations (3) and (6–11) are subject to the following boundary conditions:

$$U_l|_{x=0} = U_v|_{x=0} = 0, \qquad r|_{x=0} = r_0$$
$$P_v|_{x=0} = P_{\mathrm{sat}}, \qquad P_l|_{x=0} = P_{\mathrm{sat}} - \frac{\sigma_l}{r_0} \tag{13}$$

where r_0 is the radius at the top of the cuvette, and P_{sat} is the saturation vapor pressure of pentane at the experimentally measured temperature of the condenser region. The pressure of the vapor remains almost constant because of the large volume of the bubble as compared with the liquid channel in the corner meniscus, even with the wide variation in densities of the two phases. The initial pressure in the liquid is given by the pressure in the vapor less the interfacial tension due to surface tension.

In Eqs. (6) and (7) there is an evaporative heat flux term q_e, which is an unknown. This heat enters the liquid via the solid quartz substrate, since the solid has a much higher conductivity and area than the liquid. Thus, the heat from the heater flows through the quartz into the liquid, causing the liquid to evaporate. The vapor then transports the heat as internal latent heat and releases it in the cooler end. Solving the heat equation in the solid will provide us with the

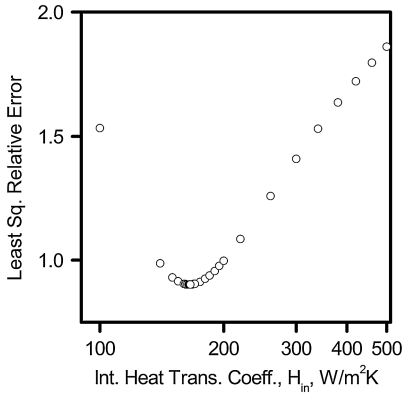

Fig. 19 Convergence for H_{in}. The error represents the sum of relative squared error between the radius and temperature measurements with their respective model-predicted values. A simple search algorithm was used to determine the best fit.

unknown q_e. To solve for the heat flow in the solid, a two-dimensional finite element model (FEM) of the solid quartz cuvette was developed. Figure 20a shows the 2-D heat transfer model developed with the various boundary conditions. At the top ($X = 0$ and $Y = 0$ to 1.25), there is a heat input of Q_{in} of Q W/(5.5 mm)^2, which represents the net heat supplied to the solid, where Q is the total heater input, e.g., 0.4 W. The inside of the solid in contact with the liquid meniscus has an unknown internal heat transfer coefficient of h_{in}. The outside convective heat transfer coefficient is h_{out} and equal to 8 W/m^2 K and has been obtained from correlations for a flat surface with natural convection. Radiation to the ambient was also included on this surface, since quartz has a high emissivity (assumed to be 1 here) for thermal radiation. The temperature at the bottom is taken as the experimentally measured temperature T_{bot}. Thus, the heat equation in the solid can be solved and the net heat flux into the liquid at the inside surface of the solid can be determined. Under these boundary conditions, the heat flux into the liquid changes sign, as shown in Fig. 20, in which the positive portion represents the evaporator, and the negative portion corresponds to the condenser. Once the q_e is known as a function of the axial distance X, it can be used to calculate the meniscus radius r. The outside surface of the solid provides us with the temperature distribution that can be compared with the experimentally measured temperature. The value of h_{in} is determined using a simple search algorithm. An initial range of h_{in} is chosen and divided into 10 equal sections. For each value of h_{in}, the relative error between the meniscus radius and external temperature and their corresponding model-predicted values are squared and summed to provide the error estimate. Then the range of h_{in} is decreased to the region corresponding to the two minimum error values obtained, as shown in Fig. 19; this process is repeated in the new range, and so on. Progressively smaller ranges in which to search for h_{in} to minimize the relative error are obtained. The variation in error was very small after the fourth iteration, and the h_{in} corresponding to this was selected; in our case, this was calculated to be 165.0 W/m^2 K. The reader is reminded that this is simply the heat transfer coefficient associated with the inside surface of the quartz and should not be confused with the evaporative heat transfer coefficient. Wang [25] obtained an inside heat transfer coefficient from the surface of the meniscus. If it is assumed that all the heat leaving the inside quartz surface is conducted to the meniscus surface, then values given by Wang can be scaled by the ratio of the surface area of the meniscus to the surface area of the quartz surface.

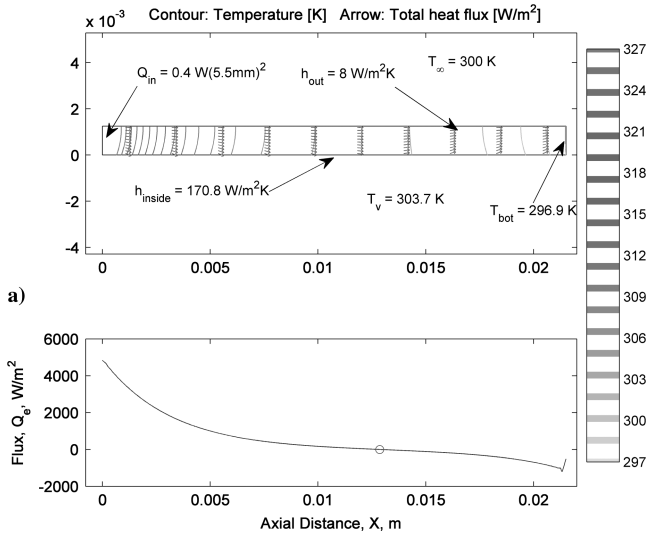

a)

b)

Fig. 20 Plots of a) FEM solution to the heat transfer problem in the solid for a heater input of 0.4 W (inside surface represents the solid–liquid interface) and b) heat transfer profile given by the FEM model. The circle represents the location of zero heat flux, i.e., where the flux changes sign, indicating a switch from the evaporator to the condenser region.

Thus scaled, the heat transfer coefficients match with the values presented here.

Figure 21a compares the radius calculated with the experimentally measured values, and Fig. 21b compares the external temperature experimentally measured with that predicted by the 2-D FEM model. There is some agreement between the observed and calculated values. The microconvection setup due to the presence of the central drop in zone 4 causes the disagreement near the 6 mm axial location. The drop could be forming due to Marangoni flows that are set up due to the temperature gradient between the corner and the flat face of the quartz surface. These ideas are being further investigated by using higher magnifications and by studying transient behavior. The location of the condenser region is determined in the model as the point at which the heat flux changes sign from positive to negative. It was found that the calculated value was 12.69 mm, and the experimentally measured value was 14 mm. The location of the condenser, as determined from the image data, was 12.11 mm. Note that the experimentally determined location is given by the thermocouple position.

Figure 22 shows the variation in pressure in the vapor and the liquid phases along the length of the cuvette. There is very small variation in the vapor pressure, since the volume of the vapor is relatively large. The liquid pressure, on the other hand, shows some variation that is due to the effect of both hydrostatics and the suction generated by surface tension as it pulls the liquid up (toward the left of the figure). Figure 23 shows the variation of the average liquid and vapor velocities. The negative value of the liquid velocity indicates that it is traveling up toward the evaporator, and the positive value of the vapor indicates that it is traveling to the condenser. Note that the

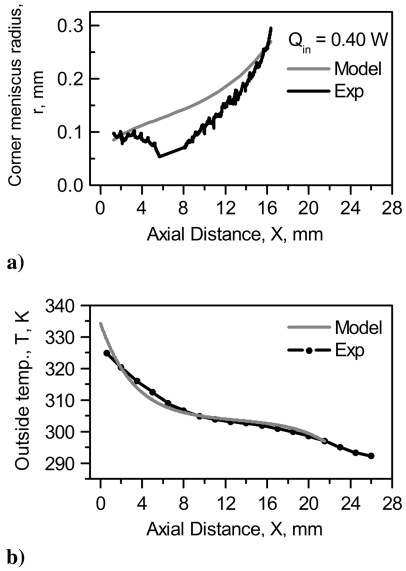

a)

b)

Fig. 21 Plots of a) comparison between the experimentally measured meniscus radius and that obtained from the model and b) external temperature profile on the quartz cuvette surface compared with that predicted by the model; $Q_{\text{in}} = 0.40$ W.

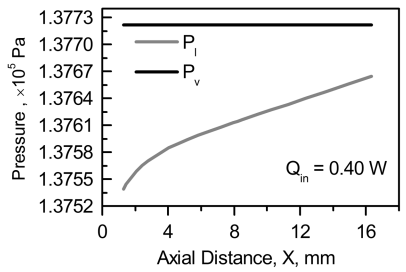

Fig. 22 Pressure in the liquid and vapor phases as obtained from the model.

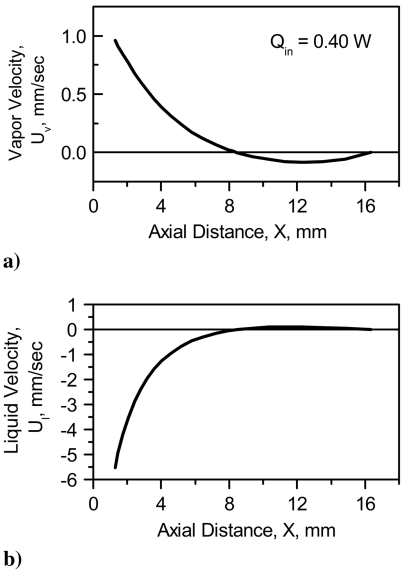

Fig. 23 Plots of a) vapor-phase and b) liquid-phase velocities obtained from the model.

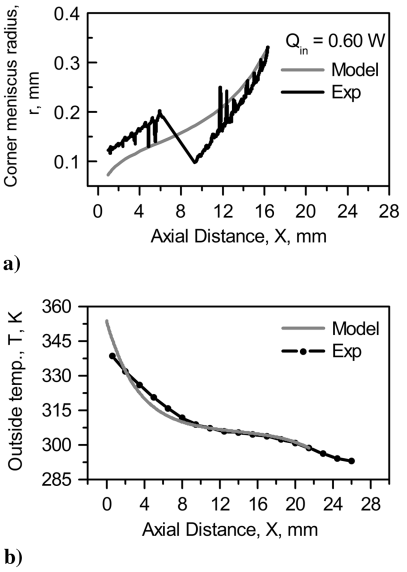

Fig. 25 Plots of a) comparison between the experimentally measured meniscus radius and that obtained from the model and b) external temperature profile on the quartz cuvette surface compared with that predicted by the model; $Q_{in} = 0.60$ W.

velocities change sign near the condenser region, indicating a reversal of flow direction.

The heat loss to the surrounding from the outside surface of the cuvette had two components: the convective heat transfer and the radiative heat transfer (Fig. 24a). Radiative heat transfer is very important for the CVB experiment because, apart from the conduction of the heat through the quartz substrate, it will be the major heat-loss mechanism in the space environment, in which there is no gravity and hence no convection. It was found that about 30% of the heat loss to the surroundings happens through radiation, as shown in Fig. 24b.

A second set of results for the heat input of 0.60 W is shown in Fig. 25 for the case of $Q_{in} = 0.60$ W. As before, an optimization was done to determine the value of h_{in}, which was 150.8 $\mathrm{W/m^2\,K}$. There is good agreement between the experimental values and those predicted by the model.

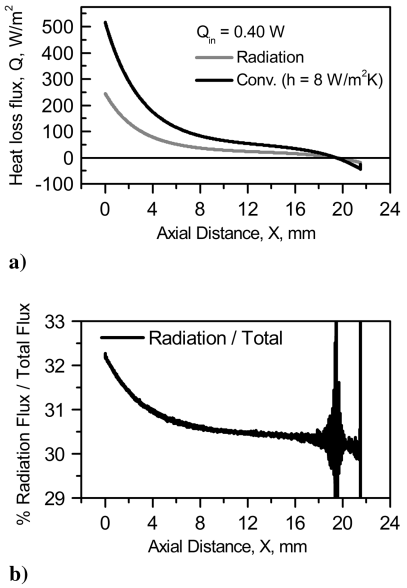

Fig. 24 External heat loss from the exposed surface of the cuvette: a) contribution by the convective and the radiative heat loss and b) relative contribution by radiation. Values near the inflection point should be ignored as they are ratios of two small numbers.

The model developed here is a relatively simple model for the heat pipe and it does an adequate job of explaining the experimental observations. It does not use the simplifications such as constant heat flux, but uses a finite element model to obtain the heat flux. It was also established that radiation is important for heat loss. The finite element model supplied the inside heat transfer coefficient, which was optimized to get the best possible agreement with the experimental values.

V. Conclusions

Ground-based experimental studies were done using the flight hardware as a baseline with which results from microgravity taken aboard the International Space Station will be compared.

The following conclusions can be drawn from this work:

1) Isothermal data agreed very well with existing theoretical predictions.

2) Nonisothermal data also agreed well with our present understanding of the wickless heat pipe. Zones were identified and it was possible to locate the different regions, i.e., evaporator and condenser regions, of the heat pipe.

3) Temperature and pressure measurements were done that were consistent with each other. It was possible to locate the position of the beginning of the condenser from temperature data, and the vapor pressure of pentane at that location correlated well with the experimentally measured vapor pressure. The location of the condenser determined optically coincided with that obtained from temperature measurements.

4) Oscillations were inferred to be occurring at higher values of heat flux.

5) A model was developed to predict the radius of curvature as a function of axial distance. The model requires knowledge of the heat flux from the solid quartz to the liquid meniscus. This was obtained by solving a 2-D heat transfer model of the solid using the finite element method.

6) The microscale interferometry data and observations obtained using higher magnification indicate that complex gravity-induced microconvection is present in the vapor. Complementary data to be obtained on the ISS will be used to further this hypothesis.

Further investigations are underway on other cuvettes. More comprehensive models are also under development. Studies are also being made to determine the reason for the formation and behavior of the various zones identified in this work.

Acknowledgments

This material is based on the work supported by NASA under grant no. NNX09AL98G. Any opinions, findings, and conclusions or recommendations expressed in this publication are those of the authors and do not necessarily reflect the views of NASA.

References

[1] Peterson, G. P., *An Introduction to Heat Pipes: Modeling, Testing, and Applications*, Wiley-Interscience, New York, 1994.

[2] Bowman, W. J., Winn, R. C., and Martin, H. L., "Transient Heat-Pipe Modeling—A Quasisteady, Incompressible Vapor Model," *Journal of Thermophysics and Heat Transfer*, Vol. 6, No. 3, July–Sept. 1992, pp. 571–574.
doi:10.2514/3.406

[3] Launay, S., Sartre, V., and Lallemand, M., "Hydrodynamic and Thermal Study of a Water-Filled Micro-Heat-Pipe Array," *Journal of Thermophysics and Heat Transfer*, Vol. 18, No. 3, 2004, pp. 358–363.
doi:10.2514/1.11781

[4] Suman, B., De, S., and DasGupta, S., "A Model of the Capillary Limit of a Micro Grooved Heat Pipe and the Prediction of Dry Out Length," *International Journal of Heat and Fluid Flow*, Vol. 26, No. 3, 2005, pp. 495–505.
doi:10.1016/j.ijheatfluidflow.2004.09.006

[5] Ma, H. B., Peterson, G. P., and Lu, X., "The Influence of Vapor-Liquid Interactions on the Liquid Pressure Drop in Triangular Microgrooves," *International Journal of Heat and Mass Transfer*, Vol. 37, No. 15, 1994, pp. 2211–2219.
doi:10.1016/0017-9310(94)90364-6

[6] Babin, B. R., Peterson, G. P., and Wu, D., "Steady-State Modeling and Testing of a Micro Heat Pipe," *Journal of Heat Transfer*, Vol. 112, No. 3, 1990, pp. 595–601.
doi:10.1115/1.2910428

[7] Ha, J. M., and Peterson, G. P., "Analytical Prediction of the Axial Dryout Point for Evaporating Liquids in Triangular Microgrooves," *Journal of Heat Transfer*, Vol. 116, No. 2, 1994, pp. 498–503.
doi:10.1115/1.2911428

[8] Khrustalev, D., and Faghri, A., "Thermal Analysis of a Micro Heat Pipe," *Journal of Heat Transfer*, Vol. 116, No. 1, 1994, pp. 189–198.
doi:10.1115/1.2910855

[9] Longtin, J. P., Badran, B., and Gerner, F. M., "A One-Dimension Model of a Micro Heat Pipe During Steady-State Operation," *Journal of Heat Transfer*, Vol. 116, No. 3, 1994, pp. 709–715.
doi:10.1115/1.2910926

[10] Khrustalev, D., and Faghri, A., "Heat Transfer During Evaporation on Capillary Grooved Structures of Heat Pipes," *Journal of Heat Transfer*, Vol. 117, No. 3, 1995, pp. 740–747.
doi:10.1115/1.2822638

[11] Peterson, G. P., and Ma, H. B., "Theoretical Analysis of the Maximum Heat Transport in Triangular Grooves: A Study of Idealized Micro Heat Pipes," *Journal of Heat Transfer*, Vol. 118, No. 3, 1996, pp. 731–739.
doi:10.1115/1.2822693

[12] Peterson, G. P., and Ha, J. M., "Capillary Performance of Evaporating Flow in Micro Grooves: An Approximate Analytical Approach and Experimental Investigation," *Journal of Heat Transfer*, Vol. 120, No. 3, 1998, pp. 743–751.
doi:10.1115/1.2824344

[13] Bowman, W. J., Moss, T. W., Maynes, D., and Paulson, K. A., "Efficiency of a Constant-Area, Adiabatic Tip, Heat Pipe Fin," *Journal of Thermophysics and Heat Transfer*, Vol. 14, No. 1, 2000, pp. 112–115.
doi:10.2514/2.6497

[14] Rag, R. L., and Sobhan, C. B., "Computational Analysis of Fluid Flow and Heat Transfer in Wire-Sandwiched Microheat Pipes," *Journal of Thermophysics and Heat Transfer*, Vol. 23, No. 4, 2009, pp. 741–751.
doi:10.2514/1.44101

[15] Kobayashi, Y., Ikeda, S., and Iwasa, M., "Evaporative Heat Transfer at the Evaporative Section of a Grooved Heat Pipe," *Journal of Thermophysics and Heat Transfer*, Vol. 10, No. 1, 1996, pp. 83–89.
doi:10.2514/3.756

[16] Ma, H. B., and Peterson, G. P., "Temperature Variation and Heat Transfer in Triangular Grooves with an Evaporating Film," *Journal of Thermophysics and Heat Transfer*, Vol. 11, No. 1, 1997, pp. 90–97.
doi:10.2514/2.6205

[17] Chang, M. J., Chow, L. C., Chang, W. S., and Morgan, M. J., "Transient Behavior of Axially Grooved Heat Pipes with Thermal Energy Storage," *Journal of Thermophysics and Heat Transfer*, Vol. 6, No. 2, 1992, pp. 364–370.
doi:10.2514/3.368

[18] Zheng, L., Wang, Y. X., Plawsky, J. L., and Wayner, P. C., "Accuracy of Measurements of Curvature and Apparent Contact Angle in a Constrained Vapor Bubble Heat Exchanger," *International Journal of Heat and Mass Transfer*, Vol. 45, No. 10, 2002, pp. 2021–2030.
doi:10.1016/S0017-9310(01)00306-4

[19] Huang, J., Plawsky, J., and Wayner, P. C., Jr., "Modeling Transport Processes in a Constrained Vapor Bubble Under Microgravity Conditions," *AIP Conference Proceedings*, Vol. 504, American Inst. of Physics, Melville, NY, 2000, p. 261.

[20] Basu, S., Plawsky, J. L., and Wayner, P. C., "Experimental Study of a Constrained Vapor Bubble Fin Heat Exchanger in the Absence of External Natural Convection," *Annals of the New York Academy of Sciences*, Vol. 1027, No. 1, 2004, pp. 317–329.
doi:10.1196/annals.1324.027

[21] Wong, H., Morris, S., and Radke, C. J., "Three-Dimensional Menisci in Polygonal Capillaries," *Journal of Colloid and Interface Science*, Vol. 148, No. 2, 1992, pp. 317–336.
doi:10.1016/0021-9797(92)90171-H

[22] Karthikeyan, M., Huang, J., Plawsky, J., and Wayner, P. C., Jr., "Experimental Study and Modeling of the Intermediate Section of the Nonisothermal Constrained Vapor Bubble," *Journal of Heat Transfer*, Vol. 120, No. 1, 1998, p. 166.
doi:10.1115/1.2830040

[23] Huang, J., "Modeling the Transport Processes in a Constrained Vapor Bubble.," Ph.D. Thesis, Chemical Engineering Dept., Rensselaer Polytechnic Inst., Troy, NY, 1998.

[24] Ayyaswamy, P. S., Catton, I., and Edwards, D. K., "Capillary Flow in Triangular Grooves," *Journal of Applied Mechanics*, Vol. 41, No. 2, 1974, pp. 248–265.

[25] Wang, Y. X., "A Study of the Vertical Constrained Vapor Bubble," Ph.D. Thesis, Chemical Engineering Dept., Rensselaer Polytechnic Inst., Troy, NY, 2001.